

## MATERIALS SCIENCE

## Reconfigurable 4D printing via mechanically robust covalent adaptable network shape memory polymer

Honggeng Li<sup>1,2,3</sup>, Biao Zhang<sup>4</sup>, Haitao Ye<sup>1,2,5</sup>, Bingcong Jian<sup>1,2</sup>, Xiangnan He<sup>1,2</sup>, Jianxiang Cheng<sup>1,2</sup>, Zechu Sun<sup>1,2</sup>, Rong Wang<sup>1,2</sup>, Zhe Chen<sup>1,2</sup>, Ji Lin<sup>6,7</sup>, Rui Xiao<sup>7</sup>, Qingjiang Liu<sup>1,2</sup>, Qi Ge<sup>1,2\*</sup>

4D printing enables 3D printed structures to change shape over “time” in response to environmental stimulus. Because of relatively high modulus, shape memory polymers (SMPs) have been widely used for 4D printing. However, most SMPs for 4D printing are thermosets, which only have one permanent shape. Despite the efforts that implement covalent adaptable networks (CANs) into SMPs to achieve shape reconfigurability, weak thermo-mechanical properties of the current CAN-SMPs exclude them from practical applications. Here, we report reconfigurable 4D printing via mechanically robust CAN-SMPs (MRC-SMPs), which have high deformability at both programming and reconfiguration temperatures (> 1400%), high  $T_g$  (75°C), and high room temperature modulus (1.06 GPa). The high printability for DLP high-resolution 3D printing allows MRC-SMPs to create highly complex SMP 3D structures that can be reconfigured multiple times under large deformation. The demonstrations show that the reconfigurable 4D printing allows one printed SMP structure to fulfill multiple tasks.

## INTRODUCTION

Four-dimensional (4D) printing is an advanced manufacturing technology that uses 3D printing technology to create 3D structures capable of changing their shapes over the fourth dimension—“time” in response to external environmental stimuli such as heat (1, 2), light (3, 4), moisture (5, 6), or electric/magnetic field (7, 8). Because of its remarkable capability of realizing seamless integration between actuators and structures, 4D printing has found great potentials in various applications, including aerospace (9, 10), biomedical (11, 12), soft robots (1, 3, 4, 13), and others (8, 14). Various 3D printing technologies have shown the possibilities of being used to realize 4D printing. They mainly include fused deposition modeling (11, 15), inkjet (13, 16–18), direct ink writing (5, 19), two-photon polymerization (14), and digital light processing (DLP) (1, 6, 10, 20). Among them, DLP enables fabrication of 3D structures with high resolution and large area (21), and thus has been widely adopted for 4D printing. To achieve 4D printing, we need to print 3D structures with environmental responsive smart materials, which mainly include hydrogels (5, 6), liquid crystal elastomers (19, 22), and shape memory polymers (SMPs) (1, 9–11, 14–18, 20). Compared with others, because of higher modulus and good compatibility with various 3D printing technologies (10), SMP-based 4D printing has been intensively studied and widely used in various applications including deployable structures (9, 10), minimal invasive surgery devices (1, 11), stiffness variable robots (13, 23), and others (8, 14). However, the majority of the SMPs used for 4D printing are thermosets where the polymer chains are covalently cross-linked in a network form.

Thus, once the SMP structure is printed, the cross-linked polymer networks are permanently set and unchangeable. In this case, one printed SMP structure only has one permanent shape, which is determined by the printing process. It is always desired that one printed SMP structure can be reconfigured to multiple permanent shapes to fulfill various tasks.

Covalent adaptable networks (CANs) are chemically cross-linked polymer networks that can change their molecular topology through bond exchange reactions (BERs) (24, 25). The cross-linked networks endow the CANs with the characteristics of thermosets, such as high-temperature mechanical, thermal, and environmental resistance (24), whereas the BERs allow the CANs to behave like thermoplastics, which can be reshaped and reprocessed when the BERs are activated. Recently, many efforts have been made to implement CAN into SMPs to achieve the shape reconfiguration. Here, we define shape reconfigurability as the capability of reconfiguring the permanent shapes of SMP through BERs. These CAN-enabled reconfigurable SMPs can be named as thermadapt SMPs to distinguish them from thermoplastic SMPs and thermoset SMPs, and emphasize the unique material behavior, i.e., thermal adaptability (26). A series of remarkable reconfigurable SMPs have been realized by incorporating thermally or optically induced BERs into the crystalline SMP systems, which mainly consist of high molecular weight linear chains such as polycaprolactone (27–31), polyurethane (32–35), polyethylene glycol (36, 37), and others (38–40). These crystalline SMP systems exhibit excellent stretchability at programming temperature (failure strain, 140 to 1200%; table S1 and fig. S1). However, the low room temperature modulus (usually less than 60 MPa; table S1 and fig. S2) and low shape-fixing temperature (at or lower than 0°C; table S1 and fig. S3) resulted from the crystallization-based shape memory effect (SME) greatly hinder them to practical engineering applications, which require the temporary shapes to be fixed at room temperature, and the shape-fixed structures to carry heavy load. High molecular weight of the crystalline SMP leads to high viscosity of the precursor solution, which is not suitable for DLP 3D printing unless the precursor solution is diluted by organic solvent (29). Other than crystalline SMPs, CANs have also been implemented to amorphous SMPs to realize the

Copyright © 2024 The Authors, some rights reserved; exclusive licensee American Association for the Advancement of Science. No claim to original U.S. Government Works. Distributed under a Creative Commons Attribution NonCommercial License 4.0 (CC BY-NC).

<sup>1</sup>Shenzhen Key Laboratory of Soft Mechanics & Smart Manufacturing, Southern University of Science and Technology, Shenzhen, China. <sup>2</sup>Department of Mechanical and Energy Engineering, Southern University of Science and Technology, Shenzhen, China. <sup>3</sup>School of Advanced Engineering, Great Bay University, Dongguan, China. <sup>4</sup>Xi'an Institute of Flexible Electronics, Northwestern Polytechnical University, 127 West Youyi Road, Xi'an, China. <sup>5</sup>Department of Mechanical Engineering, City University of Hong Kong, Kowloon, Hong Kong SAR, China. <sup>6</sup>Center for Mechanics Plus under Extreme Environments, School of Mechanical Engineering and Mechanics, Ningbo University, Ningbo, China. <sup>7</sup>State Key Laboratory of Fluid Power and Mechatronic System, Department of Engineering Mechanics, Zhejiang University, Hangzhou, China.

\*Corresponding author. Email: geq@sustech.edu.cn

shape reconfigurability (41, 42). Since the SME is achieved through glass transition, those reconfigurable amorphous SMPs can fix the temporary shape at room temperature due to the high glass transition temperature ( $T_g$ , above 50°C; table S1 and fig. S3), and high room temperature modulus (~1 GPa; table S1 and fig. S2). Moreover, the low viscosity of the precursor solution allows them to be compatible with DLP 3D printing to realize high-resolution and reconfigurable 4D printing. However, the highly cross-linked networks make those SMPs not highly deformable at programming temperature (failure strain above  $T_g$ , less than 40%; table S1 and fig. S1) (41, 42), which excludes them from the applications requiring large shape changes. Thus, it is desired to develop mechanically robust and highly ultraviolet (UV)-curable CAN-SMPs that are highly deformable at both programming and reconfiguration temperatures, and have high transition temperature and high room temperature modulus to remove the obstacles of implementing reconfigurable 4D printing of SMPs to engineering applications.

Here, we report reconfigurable 4D printing by developing mechanically robust CAN-SMPs (MRC-SMPs), which are compatible with DLP 3D printing to fabricate SMP 3D structures that can be reconfigured to multiple permanent shapes. Compared with previous reported CAN-SMPs, our MRC-SMP system are superior in the following three aspects: (i) high deformability at both programming and reconfiguration temperatures (failure strain, 1640 and 1471%, respectively), which allow the SMP to be reprogrammed and reconfigured multiple times under large deformation; (ii) high  $T_g$  (75°C) and high room temperature modulus (1.06 GPa), which allow the temporary shape to be fixed at room temperature and support heavy load; (iii) low viscosity (0.2 Pa·s) and high photoreactivity (gelation time, 4.5 s per 100  $\mu\text{m}$ ), which make the developed MRC-SMP system compatible with DLP 3D printing to fabricate highly complex 3D shape memory (SM) structures that can be reconfigured into multiple shapes under large deformation. In addition, the MRC-SMP also exhibits excellent weldability so that the separate MRC-SMP parts can be merged into one intact piece after heat treatment. To demonstrate the excellent reconfigurability and weldability of the 3D printable MRC-SMP, we present a number of applications: reconfigurable SM hinges that have microchannels for joule heating, reconfigurable SM lattice structures that are welded together to form a robotic gripper, a shape-programmable high-heel shoe that is manufactured by assembling all separately printed parts, and SM origami structures that are printed in flat form and can be reshaped into various 3D shapes. The development of MRC-SMP substantially simplifies the means of manufacturing shape-morphing structures and adds values to the 4D printing technology by imparting reconfigurability and weldability to 3D printed SMP structures.

## RESULTS

### Illustration and demonstration of reconfigurable and weldable MRC-SMPs

Figure 1 (A to C) illustrates the mechanism to achieve multiple configurations of the MRC-SMP developed in this work. Figure 1A depicts the procedure to complete one SM cycle for an as-prepared MRC-SMP square sample (configuration 1). The square sample is activated to rubbery state by heating it to a temperature above its  $T_g$  but lower than the temperature triggering BER ( $T_{\text{BER}}$ ). The temperature is referred to as programming temperature  $T_p$  ( $T_g < T_p < T_{\text{BER}}$ ). At  $T_p$ , the square sample can be readily stretched to a rectangular

one. Then, the stretched temporary shape can be fixed after cooling the sample to a low temperature ( $T_c$ ) below its  $T_g$  ( $T_c < T_g$ ), where the polymer chain mobility is greatly “frozen.” After reheating to  $T_p$ , the stretched sample recovers to its initial square shape due to the entropic elasticity. As shown in right side of Fig. 1B, the MRC-SMP sample can be reconfigured from the square shape (configuration 1) to the rectangular one (configuration 2) by stretching it at the reconfiguration temperature  $T_r$  ( $T_r > T_{\text{BER}}$ ) where BER is activated to generate new dynamic covalent bonds (DCBs), which rearrange the molecular topologies of polymer network and release the internal stress from stretching. As shown in Fig. 1B, the reconfigured MRC-SMP sample also exhibits SM behavior by following the SM cycling method as described in Fig. 1A. Because of the robust mechanical property at  $T_r$ , after multiple rounds of reconfiguration as presented in Fig. 1C, the MRC-SMP can be reconfigured to a bulged shape (configuration *i*), which also exhibits SME. Other than reconfigurability, BER also imparts weldability to the MRC-SMPs. As illustrated in Fig. 1D, two separate samples can be merged into one intact sample by welding them at  $T_r$  to trigger the BER that causes molecular rearrangement to propagate across the boundary and leads two separate parts to be chemically bonded by DCBs. The strong bonding between two parts makes the merged SMP sample also exhibit good SM behavior. To demonstrate the excellent reconfigurability and weldability of the developed MRC-SMP, as presented in Fig. 1E, we use DLP to print an “H” shape flat pattern (configuration 1), which can be programmed to a flat bridge by bending the four legs at  $T_p$  and releasing the bending loads at  $T_c$ . The flat bridge recovers to the flat pattern upon the heating to  $T_p$  (movie S1). In Fig. 1F, the flat pattern can be further reconfigured to the flat bridge (configuration 2) by bending the four legs at  $T_r$ . In configuration 2, the flat bridge can be programmed to a flat pattern in an SM cycle (movie S2). In Fig. 1G, we can also form an arch bridge (configuration 3) by cutting the four legs of the flat bridge, and then welding them to the other two sides of the bridge surface, which is bent to a curved shape at  $T_r$ . Again, the arch bridge also demonstrates a good SME (movie S3).

### Preparation and thermomechanical properties of MRC-SMP

Figure 2A presents the chemicals used to prepare the MRC-SMP precursor solution, which consists of isobornyl acrylate (IBoA) and benzyl acrylate (BA) as linear chain builder, aliphatic urethane diacrylate (AUD) as cross-linker, diphenyl(2,4,6-trimethylbenzoyl) phosphine oxide (TPO) as photoinitiator, and 1,5,7-triazabicyclo [4.4.0] dec-5-ene (TBD) as catalyst for transesterification-based BER. More details can be seen in Materials and Methods. As shown in Fig. 2B, UV radiation leads to photopolymerization of the precursor solution that converts the individual linear chain builders and cross-linkers to chemically cross-linked networks. Moreover, because of the presence of TBD, heat treatment triggers transesterification-based BER where the ester functional groups on IBoA, BA, and AUD dynamically exchange their positions (Fig. 2C) resulting in DCBs (fig. S6), which thereby endows the MRC-SMP network with reconfigurability and weldability.

We choose IBoA as the basic linear chain.  $T_g$  of the polymerized pure IBoA is 115°C (fig. S7). By adding BA into IBoA,  $T_g$  of the polymerized IBoA-BA copolymer decreases. In this work, we set the mixing ratio between IBoA and BA as 3:1, so that  $T_g$  of the IBoA-BA copolymer is about 75°C (fig. S7). We use AUD as cross-linker, because its high molecular weight ( $M_n = 31,148$ ; fig. S8) imparts high

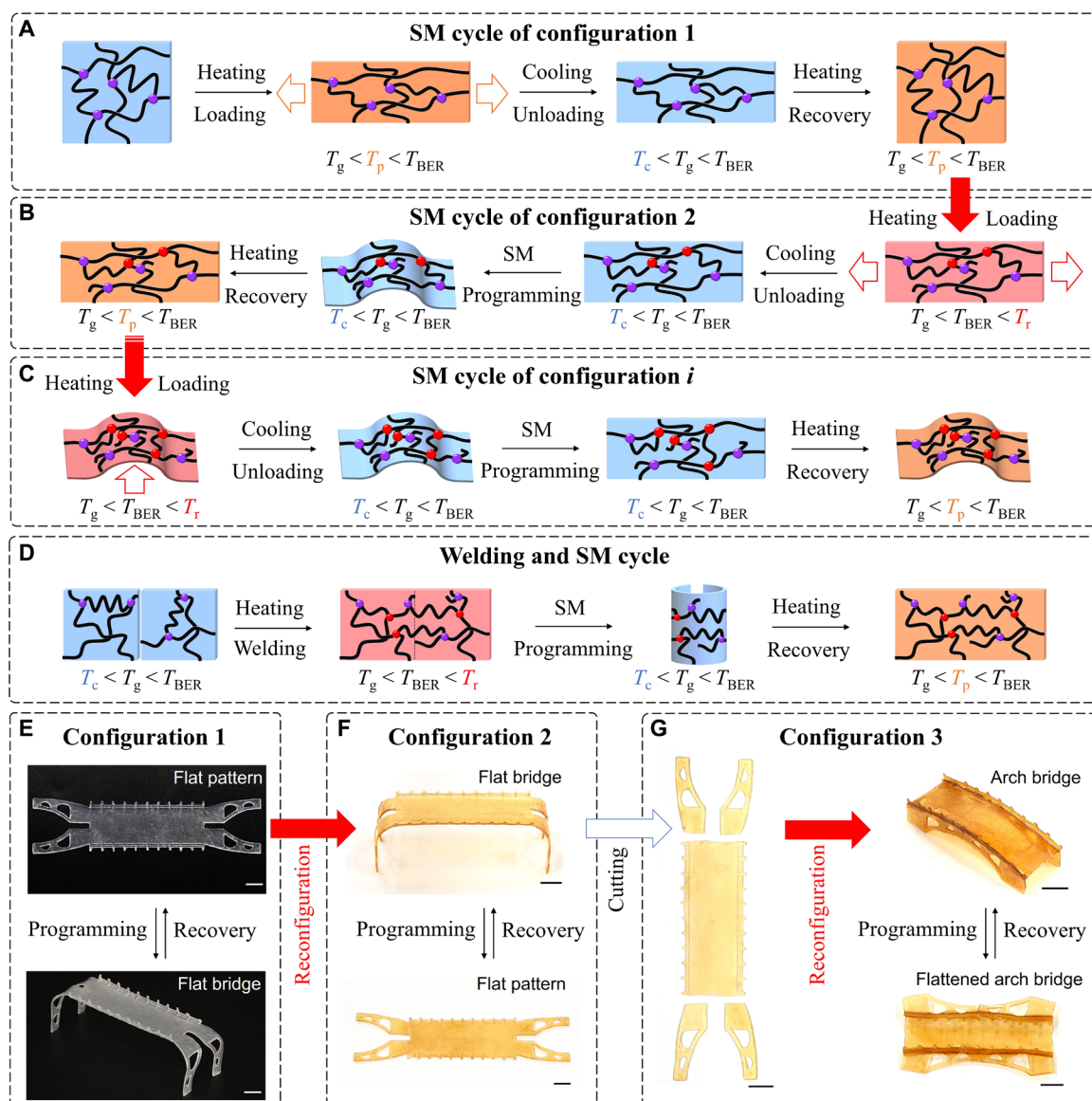


**Fig. 1. Reconfigurability and weldability of MRC-SMPs.** (A) Programming process to achieve the SM cycle for the MRC-SMP at configuration 1. (B) The MRC-SMP sample can be reconfigured to configuration 2 through BER and exhibits the SM behavior at configuration 2. (C) The MRC-SMP can be reconfigured multiple times, and the multiply reconfigured MRC-SMP also exhibits the SM behavior. (D) The SM behavior of the welded MRC-SMP sample. Purple dots in (A) to (D) are original cross-linking points. Red dots in (A) to (D) are newly generated DCBs. (E) to (G) Demonstrations of the reconfigurability and weldability of a printed MRC-SMP pattern. Scale bars, 5 mm.

rubbery-state deformability to the MRC-SMP (10, 43, 44) and facilitates kinetics of BERs (fig. S9). As shown in Fig. 2D, we perform dynamic mechanical analysis (DMA) tests to investigate the effect of AUD content on the variations of storage modulus and  $\tan\delta$  over temperature. The increasing in the AUD content from 0 to 40 wt % leads to slight rise in the rubbery-state modulus, but decrease in the glass-state modulus. In contrast, the variation of the AUD content barely affects  $T_g$ , which is indicated by the peak of  $\tan\delta$  curves. In Fig. 2E, we conduct uniaxial tensile tests to study the effect of AUD content on the stress-strain behavior of MRC-SMP samples at room temperature. The increases in the AUD content from 10 to 40 wt % results in decrease in Young's modulus from 1.42 to 0.87 GPa (fig. S10A), but notable increase in the failure strain from 4.35 to

230%. In contrast, Fig. 2F shows the increase in AUD content affects the stress-strain behavior of MRC-SMP samples at rubbery state (testing temperature,  $T_g + 30^\circ\text{C}$ ) in the opposite way. Young's modulus increases from 0.37 to 0.91 MPa (fig. S10B), but the failure strain decreases from 1120 to 290%. By synthetically considering Fig. 2 (E and F), we set AUD content as 20 wt %.

After adding TBD catalyst into the MRC-SMP samples, heat treatment triggers the transesterification-based BERs in the polymer networks. As shown in fig. S11, we perform stress relaxation tests at  $150^\circ\text{C}$  to investigate the effect of TBD content (from 0.25 to 2 wt %) on the kinetics of BER. In general, adding more TBD accelerates BER. For example, the MRC-SMP samples with 1, 1.5, and 2 wt % TBD contents need 117, 17, and 0.4 min to completely

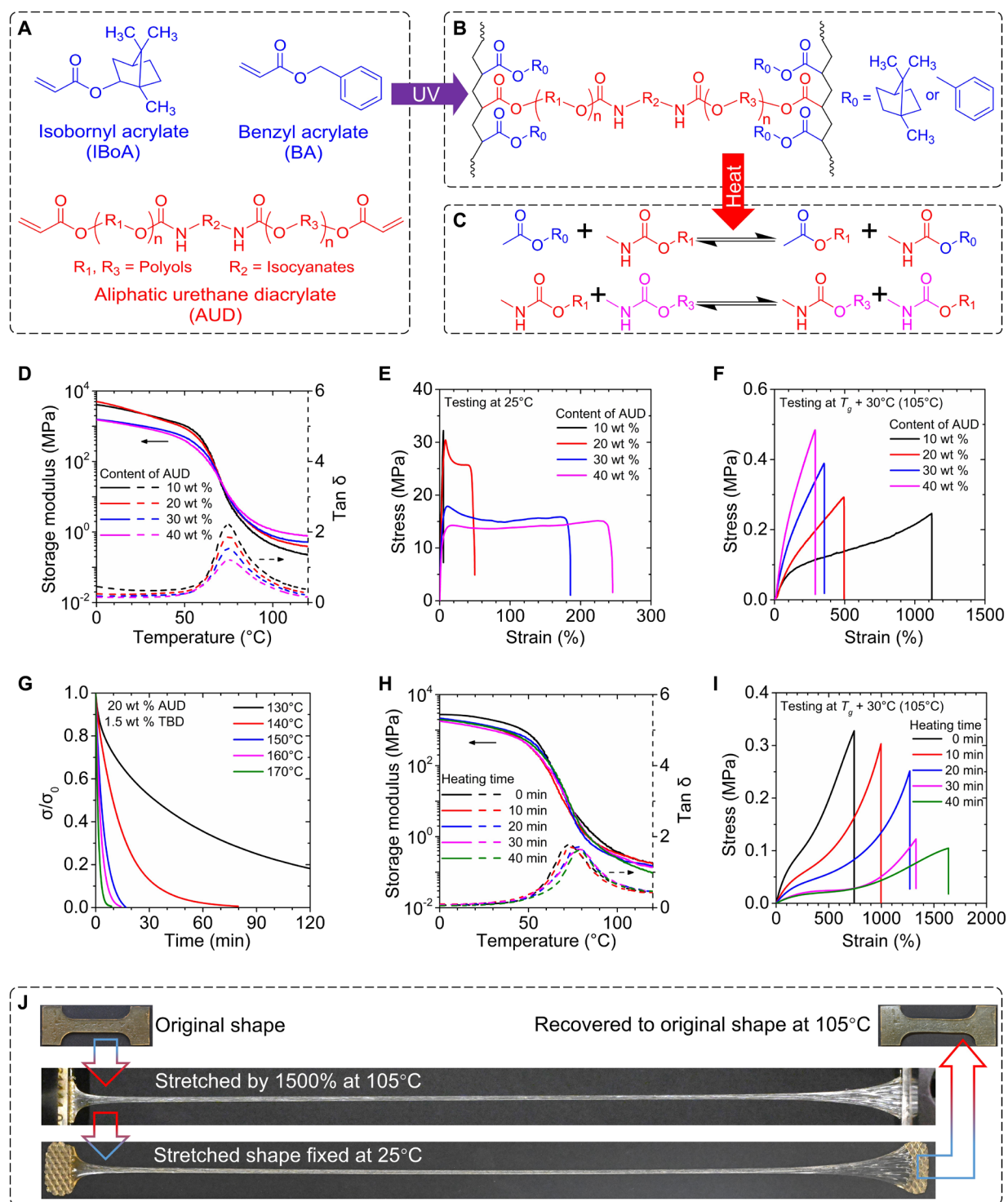


**Fig. 2. Preparation and thermomechanical properties of MRC-SMPs.** (A) Detailed chemical structures of IBoA, BA, and AUD that are used to prepare MRC-SMP precursor solution. (B) Detailed chemical structure of cross-linked MRC-SMP. (C) BER process via transesterification in MRC-SMP networks. (D) Storage modulus and tan  $\delta$  of the MRC-SMPs with different AUD contents. (E and F) Uniaxial tensile testing results of the MRC-SMPs with different AUD contents performed at 25° and 105°C, respectively. (G) Effect of temperature on stress relaxation of MRC-SMP with 20 wt % AUD and 1.5 wt % TBD. (H) Effect of heat treatment on storage modulus and tan  $\delta$  of MRC-SMPs. (I) Uniaxial tensile testing results (at 105°C) of the MRC-SMP samples thermally treated for different durations. (J) Demonstration on the high stretchability of a thermally treated MRC-SMP sample during an SM cycle.

release the stress. Moreover, we conduct uniaxial tests to investigate the effect of TBD content on the stress-strain behavior of the MRC-SMP sample at room temperature. As shown in fig. S12, the sample with 1.5 wt % TBD has the highest failure strain (103%) and relatively high modulus (1.06 GPa). By synthetically considering figs. S11 and S12, we set TBD content as 1.5 wt %. Figure 2G shows the stress relaxation tests of the MRC-SMP sample with 1.5 wt % TBD at different temperatures. It shows that higher temperature leads to faster stress relaxation. In the following experiments, we use 150°C to apply the heat treatment where the kinetics of BER is moderate and can be better controlled. We further investigate the effect of heat treatment duration on the thermomechanical behavior of the MRC-SMP samples. Figure 2H reveals that the extension on heat treatment duration barely affects the DMA curves. However, as shown in Fig. 2I, the rubbery-state stress-strain behavior is remarkably influenced by heat treatment duration. After extending heat treatment duration from 0 to 40 min, the Young's modulus decreases from 0.086 to 0.015 MPa, but the failure strain substantially increases from 741 to 1640%. Figure 2I implies that as the BERs proceed, the effective cross-linking density decreases, which leads to the reduction in Young's modulus; the average length of linear chains increases so that the sample becomes more stretchable. Figure 2J demonstrates the SM behavior of an MRC-SMP sample, which was thermally treated at 150°C for 40 min. It can be stretched by 1500% at rubbery state (at 105°C) without failure. Most stretched shape can be fixed at room temperature, and the stretched sample recovers to its original shape by heating to 105°C. In fig. S13, we compare the SM behavior of the MRC-SMP samples before and after BER. Both samples possess excellent shape fixity and recovery. In addition, we also examine the SM behaviors of the MRC-SMP (20 wt % AUD) at lower programming temperatures (fig. S14) and the MRC-SMP with different AUD contents (fig. S15). In all these cases, the MRC-SMP samples demonstrate great shape fixity and recovery.

### Reconfiguration and welding of MRC-SMP

On the basis of Fig. 2G, we set 150°C as the reconfiguration temperature where an MRC-SMP sample with 1.5 wt % TBD can completely release the applied tensile stress within 17 min. Thus, the stretchability of MRC-SMP at 150°C is critical as it reflects the reconfigurability of the MRC-SMP. In Fig. 3A, the MRC-SMP sample without heat treatment (before BER) can be stretched by 672% at 150°C. In contrast, after being heated at 150°C for 40 min (after BER), the failure strain is increased to 1471%, while the Young's modulus decreases from 77 to 47 kPa. In addition, as shown in fig. S16A, lower strain rate leads to higher stretchability at 150°C as the polymer networks have more time to proceed BERs, which relax more stretched polymer chains. Similarly, in fig. S16B, the MRC-SMP exhibits higher stretchability at higher reconfiguration temperature, which leads to faster BERs. The high stretchability at 150°C allows one MRC-SMP sample to be reconfigured under large deformations with multiple times. As shown in Fig. 3B, an MRC-SMP strip can be reconfigured four times, and the accumulated stretch ( $\lambda = L/L_0$ ;  $L_0$ , initial length;  $L$ , length after reconfiguration) applied to the strip can be as high as 16. The inset in Fig. 3B shows that the sufficient heating time at 150°C allows the applied stress at each reconfiguration step to be completely relaxed so that the reconfigured shapes can be well maintained. As shown in Fig. 3C, we further carry out small-angle x-ray scattering (SAXS) experiments to analyze the effect of BER on the molecular topology of the MRC-SMP

samples. Details on the SAXS analysis can be seen in Materials and Methods. Figure 3D presents the scattering pattern of a fresh sample without deformation, which is circular indicating that the polymer chains are randomly oriented. Figure 3E shows the scattering pattern of the fresh MRC-SMP stretched by 400%, which turns to be a diamond shape implying that the stretch in  $y$  direction causes polymer chains to be denser in  $y$  direction (45). Compared with Fig. 3D, the scattering pattern of the heat-treated sample (Fig. 3F) is also circular but has lower energy intensity at the same scattering vector  $q$ . This indicates that BER makes the polymer network less dense but still pure randomly oriented. After 400% stretch, the scattering pattern of the heat-treated sample becomes diamond shape again. The further heat treatment alters the scattering pattern of 400% stretched sample to be circular revealing that BER rearranges the molecular topology from the stretching-oriented one to the randomly oriented one. Details on the analysis of SAXS patterns can be found in fig. S17.

In Fig. 3I, we perform SM cyclic tests for the four reconfigured shapes, which all have good shape fixity and recovery (details in fig. S18). To demonstrate such remarkable reconfigurability of the MRC-SMP, in Fig. 3J, we reconfigure an MRC-SMP strip to the other four permanent shapes by folding, stretching, twisting, and imprinting. The MRC-SMP samples in the five permanent shapes all exhibit good SM behaviors (movie S4). In addition, BER also imparts weldability to the MRC-SMPs. The method on welding different MRC-SMP parts together through BERs can be found in Materials and Methods and was proposed by previous works (38, 46, 47). To investigate the interfacial robustness of the welded MRC-SMP samples, we perform lap shear tests at room temperature to compare the mechanical response of the specimen that was prepared by welding two separate parts through BER (fig. S19) with that of the specimen that was completely printed. As shown in Fig. 3K, the welded specimens exhibit nearly the same mechanical response as the fully printed specimens, which indicates that BER causes molecular topological rearrangement to propagate across the boundary and leads two separate parts to be chemically bonded to form an intact part. In addition, as presented in fig. S20, we also perform uniaxial tensile tests to investigate the interfacial robustness of the welded MRC-SMP samples, which also show that the welded specimens exhibit nearly the same mechanical response as the fully printed specimens.

### Reconfigurable 4D printing

Viscosity is one of the key properties that determine whether the MRC-SMP precursor solution is suitable for DLP 3D printing. Thus, we perform rheological tests to investigate the effect of AUD content on viscosity of the MRC-SMP precursor solutions. Detailed information on rheological tests can be found in the Materials and Methods. As shown in Fig. 4A, although the increase in the AUD content leads to the rise in viscosity, the solution with 40 wt % AUD has a viscosity of 1.01 Pa·s, which is sufficiently low for DLP 3D printing (10). In this work, all the MRC-SMPs are prepared with 20 wt % AUD whose viscosity is only 0.2 Pa·s. UV curing time is another key property that determines whether the precursor solution is suitable for DLP 3D printing. Figure 4B presents the results from photorheological tests, which shows that the precursor solution with 20 wt % AUD exhibits excellent photoactivity: UV curing a 100- $\mu\text{m}$ -thick layer with UV light intensity of 1  $\text{mW}\cdot\text{cm}^{-2}$  only takes 7.4 s, and the UV curing time can be further decreased to 4.5 s by increasing the UV light intensity to 16  $\text{mW}\cdot\text{cm}^{-2}$  (fig. S21 and Materials and Methods). In summary, Fig. 4 (A and B) confirms that the MRC-SMP

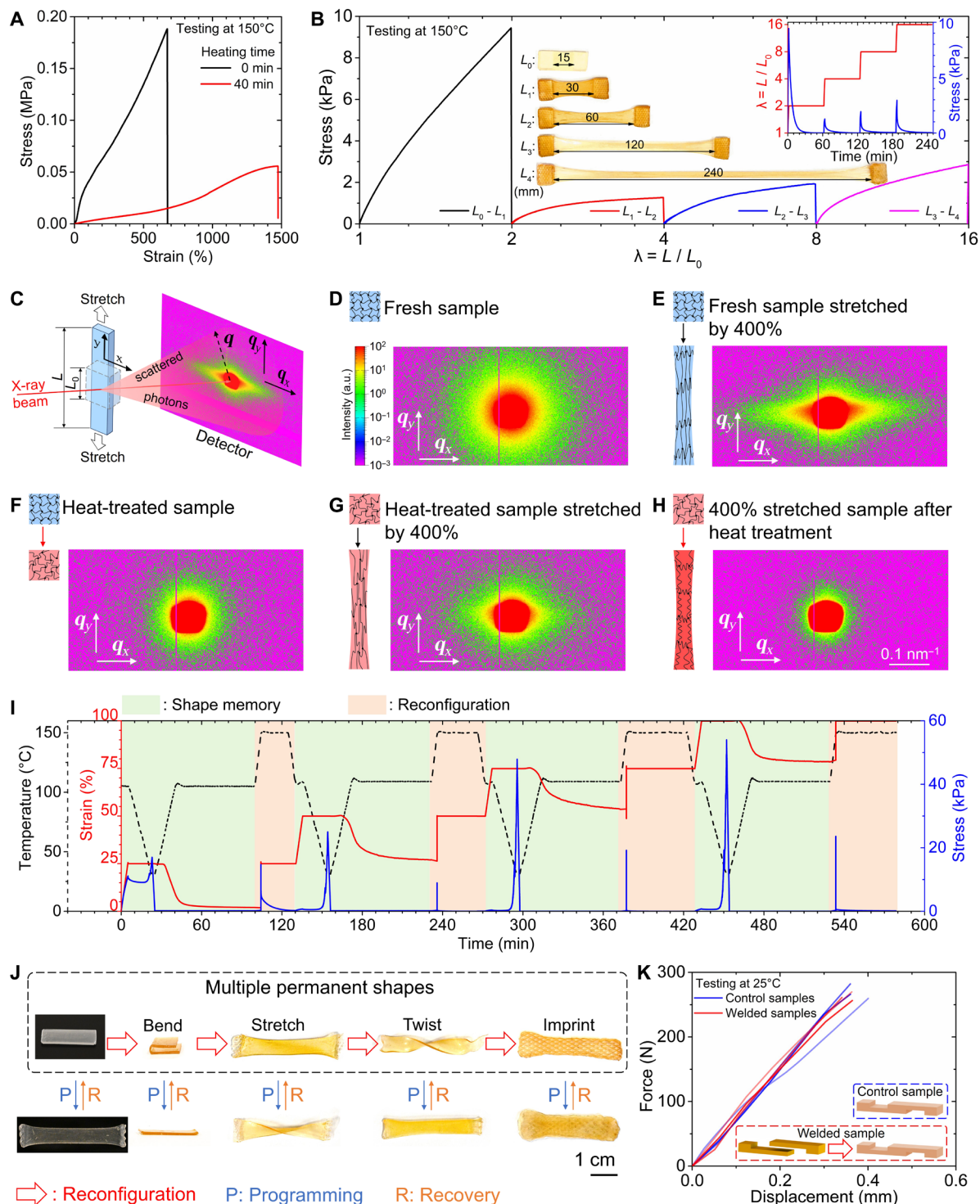


**Fig. 3. Reconfiguration and welding of MRC-SMP.** (A) Uniaxial tensile testing results of the MRC-SMP samples before and after heat treatment at 150°C. (B) Demonstration of an MRC-SMP sample that can be reconfigured to 16 times of its original length after four rounds of reconfiguration at 150°C. (C) Illustration of a SAXS test showing the relation between stretch direction on the MRC-SMP and the corresponding  $\mathbf{q}$  space of scattering pattern. (D to H) SAXS patterns from MRC-SMPs with different thermo-mechanical histories. (D) Fresh sample, (E) fresh sample stretched by 400%, (F) heat-treated sample, (G) heat-treated sample stretched by 400%, (H) 400% stretched sample after heat treatment. (I) SM-reconfiguration cyclic test of an MRC-SMP sample. a.u., arbitrary units. (J) Demonstration showing that an MRC-SMP specimen can be reconfigured to multiple permanent shapes. (K) Comparison of mechanical properties between welded specimens and fully printed specimens through lap shear tests.

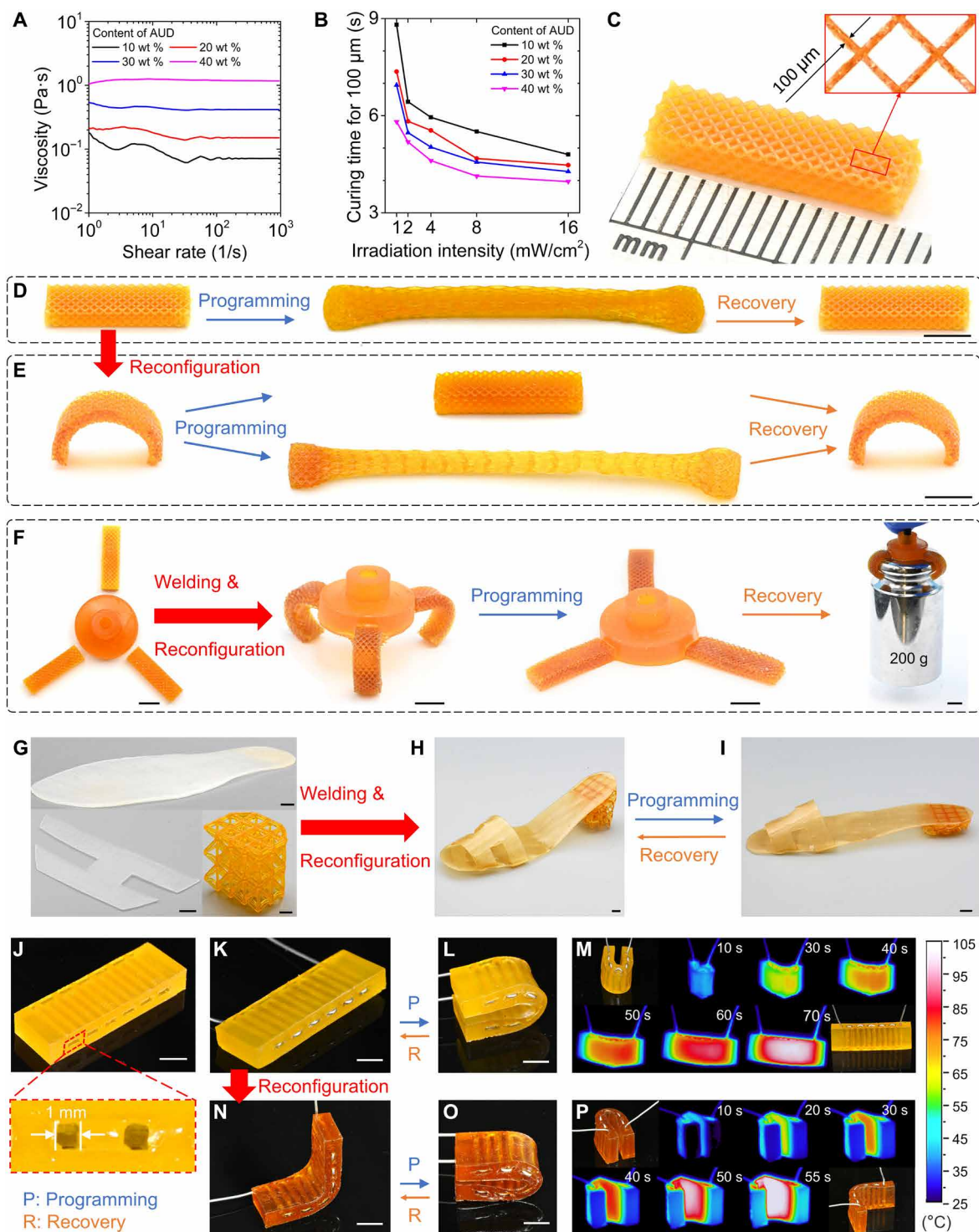


**Fig. 4. Printability and reconfigurable 4D printing of MRC-SMP.** (A) Effect of AUD content on viscosity of MRC-SMP solutions. (B) Effect of AUD content on the time to curing a 100- $\mu\text{m}$ -thick MRC-SMP layer. (C) A DLP 3D printed MRC-SMP lattice structure with refined features. (D) SM behavior of a rectangular MRC-SMP lattice structure. (E) SM behaviors of a reconfigured arc-shape MRC-SMP lattice structure. (F) A SM gripper fabricated by welding three 3D printed and reconfigured lattice structure to a printed round base. (G to I) Demonstration of a shape-changeable high-heel shoe manufactured by taking advantage of the reconfigurability and weldability of MRC-SMP. (J) Snapshot of printed flat MRC-SMP hinge with microchannels. (K) Snapshot of flat hinge assembled with resistance wire. (L) Snapshot of the folded temporary shape of the flat hinge. (M) Infrared camera images of the recovery process of the flat hinge. (N) Snapshot of right-angle hinge reconfigured from a flat hinge. (O) Snapshot of the folded temporary shape of the right-angle hinge. (P) Infrared camera images of the recovery process of the right-angle hinge. Scale bars, 5 mm.

precursor solution is suitable for DLP 3D printing. Because of the high printability, as shown in Fig. 4C, we can use MRC-SMP to print a lattice structure where the diameter of each rod is 100  $\mu\text{m}$ .

The 3D printed MRC-SMP structures exhibit excellent reconfigurability and weldability. As shown in Fig. 4D, in an SM cycle, an MRC-SMP lattice structure can maintain its stretched shape at 25°C and recover to its as-printed state after heating to 105°C (movie S5). In Fig. 4E, we can reconfigure the rectangular lattice structure to a curved one by bending it at 150°C for 20 min to relax the applied stress. The curved lattice structure also exhibits excellent deformability and SME (movie S6). Taking advantage of reconfigurability and weldability of CANs, we can achieve 3D structures, which cannot be easily manufactured by direct 3D printing. As presented in Fig. 4F, we print three the rectangular lattice structures and a circular base in one batch. Then, we can make a SM gripper by welding the three lattice structures to the base and reconfiguring them to the curved shape. The manufactured gripper can grab high-weight objects due to the SM effect and the high room temperature modulus of MRC-SMP (movie S7). It should be noted that fabricating such a gripper by printing the individual parts and welding the reconfigured lattice structures only takes 45 min. In contrast, directly 3D printing such a gripper may take 100 min, not to mention the overhang parts that are challenging for 3D printing. Moreover, the developed MRC-SMP might be beneficial to the fashion industry. As shown in Fig. 4G, we separately print the shoe sole, vamp, and lattice heel (fig. S22). Then, we make a high-heel shoe by reconfiguring and welding the three parts (Fig. 4H). The shape of the shoe can be further adjusted by using the SME (Fig. 4I and movie S8). In addition, to realize electrically controlled actuation, as shown in Fig. 4J, we print a flat MRC-SMP hinge with microchannels where a resistive wire can pass through (Fig. 4K). The flat hinge can be fixed at a fully folded state after thermomechanical programming (Fig. 4L). The unfolding can be triggered through joule heating by applying an 8 A current (Fig. 4M and movie S9). We can further reconfigure the flat hinge to a right-angle one (Fig. 4N), which can also be programmed to a fully folded shape (Fig. 4O). Again, the unfolding can be realized through joule heating (Fig. 4P and movie S10). Details on the electrically controlled hinge can be found in Materials and Methods and in fig. S23.

The excellent reconfigurability and weldability of the 3D printable MRC-SMPs may also revolutionize the means of manufacturing origami structures, which have been intensively studied (48, 49). As illustrated in Fig. 5 (A and B), we start the fabrication of an SM origami structure by printing a flat Miura origami pattern on self-built multimaterial 3D printer where the UV light engine is placed below the printing platform and irradiates digitalized UV patterns toward the printing platform that moves vertically to control the thickness of each layer (50). Between the UV light engine and printing platform, there is a glass plate supports the tough polymer precursor and MRC-SMP precursor containers and moves horizontally to deliver a needed solution for the corresponding layer. In each layer, the rigid panel parts are first printed with a tough polymer precursor (Fig. 5A), which is still glassy even at 150°C (fig. S24). Then, in Fig. 5B, the SM hinges are printed with the MRC-SMP precursor. Figure 5C presents the printed Miura origami sheet (configuration 1), which exhibits SM behavior and can be converted to a temporary 3D origami structure that would recover to the flat sheet upon heating due to SM effect (movie S11). In Fig. 5D, we can further use BER to reconfigure the flat sheet to the 3D origami structure (configuration 2), which is also shape memorable (movie S12). Moreover, the BER not only

enables the reconfiguration of the origami pattern but also strengthens the interfacial bonding between the tough polymer and MRC-SMP (fig. S25). In addition, the remarkable deformability of the MRC-SMP at the reconfiguration temperature allows one printed origami sheet to be reconfigured into multiple SM origami configurations as shown in Fig. 5 (E and F). High  $T_g$  of MRC-SMP ensures that the 3D origami structure has high stiffness at room temperature. As demonstrated in Fig. 5G, a 3D origami structure with 2 g (configuration 2) has sufficient stiffness to support a 500 g weight. Figure 5H presents the compressive tests for the origami structure in different configurations ( $i = 2, 3, \text{ and } 4$ ) at 25°C. Although the maximum force required to fully open the origami structure is dependent on the folding angle  $\theta$ , we need to apply 33.4 N to open the partially open origami structure (configuration 4 with  $\theta = 110^\circ$ ); to open a fully folded origami (configuration 3 with  $\theta = 0^\circ$ ) requires 399 N. Figure 5H confirms that origami structures with MRC-SMP hinges are competent to support heavy weights. The reconfigurability of the 3D printable MRC-SMP substantially reduces the time to fabricate 3D SM origami structures. As summarized in Fig. 5I, the estimated time required to directly print a two-material 3D origami structure in configurations notably influenced by the height of the structure. For example, it takes only 8 min to directly print the flat origami pattern in Fig. 5C; by contrast, direct printing of the origami structure in configuration 7 (Fig. 5F) requires 372 min. By taking advantage of reconfigurability of MRC-SMP, configuration 7 can also be fabricated by printing the flat origami pattern and then reconfiguring it at 150°C. The whole process only takes 28 min, including 8 min for printing the flat pattern and 20 min for manual operation and heat treatment. Furthermore, we can use 3D printing combined with reconfiguration to fabricate the 3D origami structure in any configuration including configurations 8 and 9 in Fig. 5F, which are challenging to be fully printed. The fabrication time for the combined method is independent of the geometry of 3D structure (28 min for any origami structure in Fig. 5F).

## DISCUSSION

By addressing the weak thermomechanical properties of the current CAN-SMPs, we report reconfigurable 4D printing via mechanically robust CAN-SMPs (MRC-SMPs), which have high deformability at both programming and reconfiguration temperatures, high  $T_g$ , and high room temperature modulus. The high printability allows the MRC-SMPs to be compatible with DLP high-resolution 3D printing to create highly complex SMP 3D structures that can be reconfigured multiple times under large deformation. The demonstrations show that the reconfigurable 4D printing allows one printed SMP structure to fulfill multiple tasks. In addition, the MRC-SMP also exhibits excellent weldability so that the separate MRC-SMP parts can be merged into one intact piece after heat treatment. The development of MRC-SMP greatly simplifies the means of manufacturing shape-morphing structures and adds values to the 4D printing technology by imparting reconfigurability and weldability to 3D printed SMP structures.

## MATERIALS AND METHODS

### Materials

IBoA, BA, TPO, and Sudan I were purchased from Sigma-Aldrich (Shanghai). Ebecryl 8413 (AUD) was provided by Allnex (Germany). TBD was purchased from TCI (Shanghai).

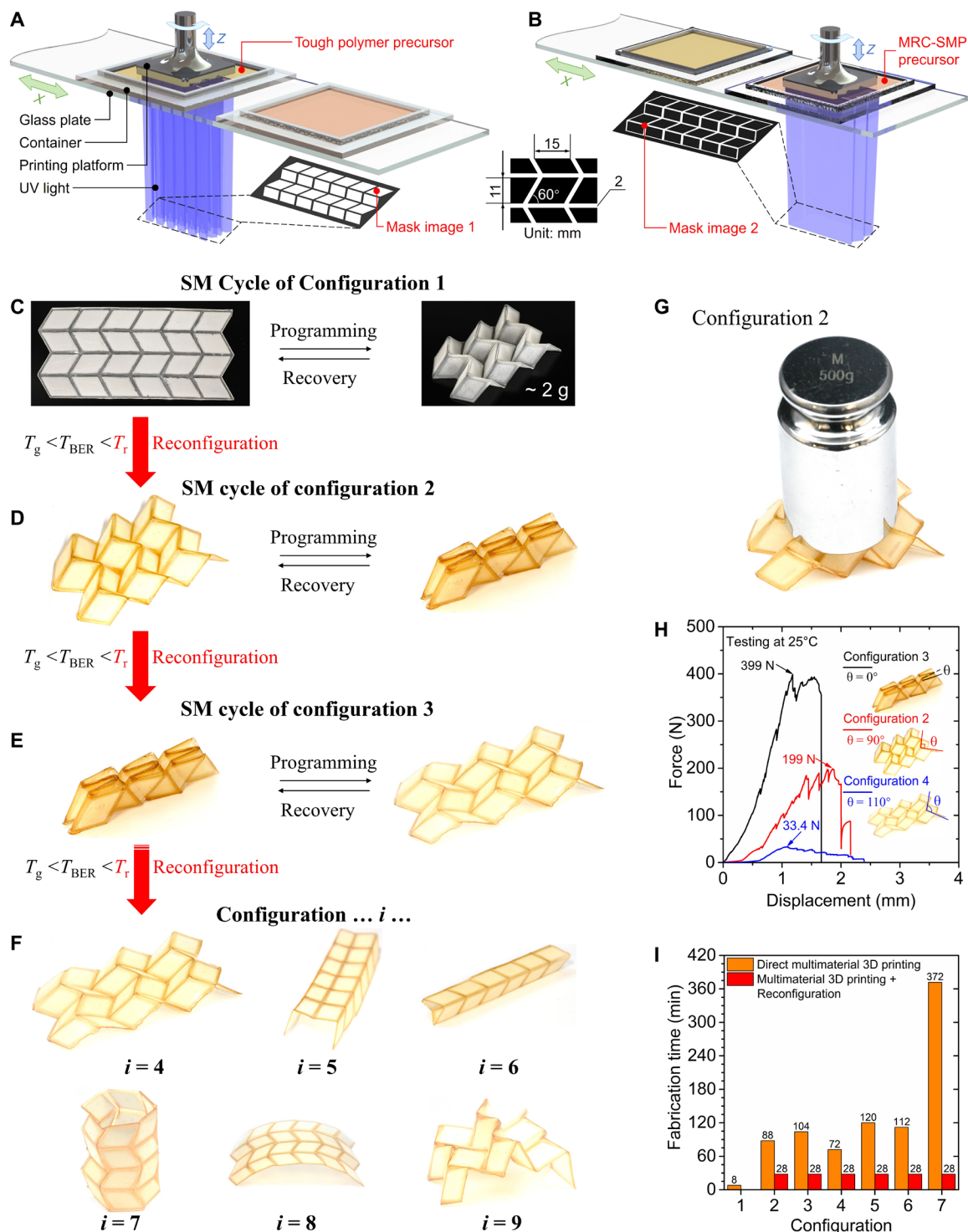


**Fig. 5. Multimaterial reconfigurable SM origami.** (A and B) Schematic of multimaterial printing reconfigurable SM origami. (C to F) Demonstrations of multiple configurations and SM behaviors of reconfigurable SM origami. (G) Snapshot of the reconfigured 3D origami carrying heavy object. (H) Compressive tests on the origami structures in different configurations at 25°C. (I) Estimated manufacturing times for various 3D origami configurations via different manufacturing methods.

### Gel permeation chromatography test

The molecular weight of AUD was measured by ACQUITY Advanced Polymer Chromatography system (Waters Corporation). The test temperature was 50°C, the eluent was *N,N*-dimethylformamide (DMF)/LiCl ( $10 \times 10^{-3}$  M), and the flow rate of the eluent was  $0.5 \text{ ml/min}^{-1}$ . The sample was prepared in DMF/LiCl and filtered through 0.20- $\mu\text{m}$  pore size polytetrafluoroethylene filter before the measurements. The test results were calibrated with polymethyl methacrylate standard (3000 to 70,000 g/mol).

### Precursor solution preparation

The IBoA-BA precursor was prepared by mixing IBoA and BA in different compositions, 2 wt % TPO of total weight of monomers was added as the photoinitiator. The MRC-SMP precursor was prepared by mixing IBoA-BA precursor (75 wt % IBoA and 25 wt % BA, as monomers) and AUD (as cross-linker) in different compositions. TPO (2 wt %) of total weight of monomers and cross-linker were added as the photoinitiator. After the above materials were mixed evenly, TBD was added as catalyst. In the case of high-precision 3D printing (Fig. 4), 0.05 wt % Sudan I of total weight of the MRC-SMP precursor was added as UV absorber to improve the printing resolution.

### DMA experiments

Dynamic mechanical properties were studied by using a DMA analyzer (Q850 DMA, TA Instruments) in the tension film mode. Samples with dimensions of  $10 \text{ mm} \times 5 \text{ mm} \times 1 \text{ mm}$  were tested at a frequency of 1 Hz and an amplitude of  $10 \mu\text{m}$ . The temperature was first equilibrated at  $-9^\circ\text{C}$  for 5 min and then gradually increased to  $150^\circ\text{C}$  at a heating rate of  $3^\circ\text{C/min}$ . The glass transition temperatures ( $T_g$ ) were assigned as the temperature at which  $\tan\delta$  value was maximum.

### Uniaxial tensile experiments

Tension experiments on dog-bone specimens with gage length of 20 mm and a cross section of  $4 \text{ mm} \times 2 \text{ mm}$  were conducted using MTS machine [testing at  $25^\circ\text{C}$ , 10-kN load cell; testing at  $T_g + 30^\circ\text{C}$  ( $105^\circ\text{C}$ ) and  $150^\circ\text{C}$ , 100 N load cell] at strain rate of  $0.01 \text{ s}^{-1}$ . Before each experiment, we first raise the temperature of the thermal chamber to the testing temperature, then put in and clamp the dog-bone specimen, and keep the testing temperature for 2 min to uniformly heat the specimen.

### SM behavior tests

Figure S4 presents the result from a typical SM cyclic test for calculating  $R_f$  and  $R_r$ . At step 1, an MRC-SMP sample is stretched to  $\epsilon_p$  ( $\epsilon_p = 100\%$  in this work) at a constant strain rate ( $0.001 \text{ s}^{-1}$ ) at  $T_p$  (i.e.,  $T_g + 30^\circ\text{C}$ ). At step 2, the sample is cooled to  $25^\circ\text{C}$  with a cooling rate of  $2.5^\circ\text{C/min}$  and held at  $25^\circ\text{C}$  for 2 min while it is kept stretched. At step 3, the external load is suddenly released at  $25^\circ\text{C}$ , and the temporary fixed strain  $\epsilon_u$  can be measured. At step 4, the sample is heated to  $T_p$  at the heating rate of  $2.5^\circ\text{C/min}$  and held at  $T_p$  for 1 hour where the recovery strain  $\epsilon_r$  is measured.

### Stress relaxation experiment

The stress relaxation experiment was tested on a DMA analyzer (Q850 DMA, TA Instruments) at the reconfiguration temperature ( $150^\circ\text{C}$ , in this work). First, the DMA machine quickly heats the sample to  $150^\circ\text{C}$ , and then uniformly stretches the sample to 100%

strain ( $\epsilon_{\text{load}}$ ). Then, the sample is maintained at 100% strain and isothermally treated at  $150^\circ\text{C}$  for 1 hour. Last, unload the external force and record the strain caused by the stress relaxation test ( $\epsilon_{\text{relax}}$ ). Figure S5 presents the result from a typical stress relaxation experiment for calculating  $R_{\text{ret}}$ .

### SAXS experiment

Xeuss 3.0 (xenocs, France) was used for SAXS experiments. Using copper target, the light tube power is 30 W, and the focal spot diameter is  $30 \mu\text{m}$ ; the maximum luminous flux at the sample is  $4.5 \times 10^8 \text{ phs/s}$ ; the detector is Eiger2R 1 M, with a single pixel size of  $75 \mu\text{m}$ .

### Rheological test

The viscosity ( $\eta$ ) of MRC-SMP precursors were measured by using a controlled-stress rheometer (DHR2, TA instruments Inc., UK) with an aluminum plate geometry (diameter, 25 mm; gap,  $100 \mu\text{m}$ ). All dynamic rheological data were checked as a function of strain amplitude to ensure that the measurements were performed in the linear domain.

### Photorheological test

The storage modulus and loss modulus of materials were measured on a DHR2 (TA instruments Inc., UK) machine with an aluminum plate geometry (diameter, 20 mm; gap,  $100 \mu\text{m}$ ). First 20 s were detected without light, then 20 s were exposed in 385-nm UV light with 1, 2, 4, 8, or  $16 \text{ mW/cm}^2$  light intensity, and more 20 s were detected after the end of exposure (fig. S16). Aluminum plate rotated at a speed of  $5 \text{ rad-s}^{-1}$  throughout the 100-s detection process. The intersection of the loss modulus and storage modulus curves is the gel point, and the corresponding time minus 20 s is the curing time.

### 3D printing

The MRC-SMP precursor was printed layer by layer exposing under UV light by DLP method. 3D structure images in STL version were first sliced into layers with the target thickness, and the printing parameters were set by using the custom LabVIEW. Here, a self-assembled DLP printer with a HR6500 light engines (wavelength, 385 nm; Wintech Digital System Technology Corp.) was used to print structures in this work. The slice thickness was  $100 \mu\text{m}$ , the exposure intensity was  $8 \text{ mW/cm}^2$ , and the exposure time of each layer was 5 s. The grid structure in Fig. 4 was printed using a commercial 3D printer (405 nm, nanoArch S130 3D printing system, BMF Material, China). After printing, the surfaces of the 3D structures obtained were cleaned with high-pressure air. Last, the structures were placed in a UV oven (365 nm, UVP, UV cross-linking agent, Upland, CA, USA) for postcuring. The multimaterial origami sheets in Fig. 5 were printed on a self-assembled multimaterial DLP-based centrifugal DLP 3D printer (50).

### Interface welding

To weld separate MRC-SMP parts, we put the two separate parts together to ensure that the same cross-sectional surfaces of the two parts in contact. The sample with two separate parts was then heated at  $150^\circ\text{C}$  for 2 hours under no external force.

### Manufacturing and experiment of electrically controlled MRC-SMP hinge

The detailed dimensions of the MRC-SMP hinge can be found in fig. S23. The resistive wire was purchased from Shenzhen Jiede

Nonferrous Metals Co. Ltd. and is a Sn-Cu alloy (Sn:Cu = 99.3:0.7) with diameter of 0.6 mm and conductivity of  $8.85 \times 10^6$  S/m. During the unfolding process, an 8 A current was applied to the resistive wire to generate joule heat, which diffused into the MRC-SMP hinge to trigger the shape recovery (unfolding process). An infrared camera (InfRec R550, Nippon Avionics Co. Ltd.) was placed in front of the hinge to record the unfolding process of the hinge and investigate the temperature variation. Moreover, the three-point bending tests were conducted to investigate the effect of resistance wire on the stiffness of MRC-SMP hinge (fig. S23).

## Supplementary Materials

### This PDF file includes:

Sections S1 to S4  
Figs. S1 to S25  
Table S1  
Legends for movies S1 to S12

### Other Supplementary Material for this manuscript includes the following:

Movies S1 to S12

## REFERENCES AND NOTES

- Q. Ge, A. H. Sakhaei, H. Lee, C. K. Dunn, N. X. Fang, M. L. Dunn, Multimaterial 4D printing with tailorable shape memory polymers. *Sci. Rep.* **6**, 31110 (2016).
- M. Zarek, M. Layani, I. Cooperstein, E. Sachyani, D. Cohn, S. Magdassi, 3D printing of shape memory polymers for flexible electronic devices. *Adv. Mater.* **28**, 4449–4454 (2016).
- H. Zeng, P. Wasylczyk, C. Parmeggiani, D. Martella, M. Burreli, D. S. Wiersma, Light-fueled microscopic walkers. *Adv. Mater.* **27**, 3883–3887 (2015).
- G. Hou, X. Zhang, F. Du, Y. Wu, X. Zhang, Z. Lei, W. Lu, F. Zhang, G. Yang, H. Wang, Z. Liu, R. Wang, Q. Ge, J. Chen, G. Meng, N. X. Fang, X. Qian, Self-regulated underwater phototaxis of a photoresponsive hydrogel-based phototactic vehicle. *Nat. Nanotechnol.* **19**, 77–84 (2024).
- A. S. Gladman, E. A. Matsumoto, R. G. Nuzzo, L. Mahadevan, J. A. Lewis, Biomimetic 4D printing. *Nat. Mater.* **15**, 413–418 (2016).
- Q. Ge, Z. Chen, J. Cheng, B. Zhang, Y.-F. Zhang, H. Li, X. He, C. Yuan, J. Liu, S. Magdassi, 3D printing of highly stretchable hydrogel with diverse UV curable polymers. *Sci. Adv.* **7**, eaba4261 (2021).
- Y. Kim, H. Yuk, R. Zhao, S. A. Chester, X. Zhao, Printing ferromagnetic domains for untethered fast-transforming soft materials. *Nature* **558**, 274–279 (2018).
- C. Ma, S. Wu, Q. Ze, X. Kuang, R. Zhang, H. J. Qi, R. Zhao, Magnetic multimaterial printing for multimodal shape transformation with tunable properties and shiftable mechanical behaviors. *ACS Appl. Mater. Interfaces* **13**, 12639–12648 (2021).
- K. Liu, J. Wu, G. H. Paulino, H. J. Qi, Programmable deployment of tensegrity structures by stimulus-responsive polymers. *Sci. Rep.* **7**, 3511 (2017).
- B. Zhang, H. Li, J. Cheng, H. Ye, A. H. Sakhaei, C. Yuan, P. Rao, Y. F. Zhang, Z. Chen, R. Wang, X. He, J. Liu, R. Xiao, S. Qu, Q. Ge, Mechanically robust and UV-curable shape-memory polymers for digital light processing based 4D printing. *Adv. Mater.* **33**, e2101298 (2021).
- C. Lin, J. Lv, Y. Li, F. Zhang, J. Li, Y. Liu, L. Liu, J. Leng, 4D-printed biodegradable and remotely controllable shape memory occlusion devices. *Adv. Funct. Mater.* **29**, (2019).
- Y. Kim, G. A. Parada, S. Liu, X. Zhao, Ferromagnetic soft continuum robots. *Sci. Robot.* **4**, eaax7329 (2019).
- Y. F. Zhang, N. Zhang, H. Hingorani, N. Ding, D. Wang, C. Yuan, B. Zhang, G. Gu, Q. Ge, Fast-response, stiffness-tunable soft actuator by hybrid multimaterial 3D printing. *Adv. Funct. Mater.* **29**, 1806698 (2019).
- W. Zhang, H. Wang, H. Wang, J. Y. E. Chan, H. Liu, B. Zhang, Y.-F. Zhang, K. Agarwal, X. Yang, A. S. Ranganath, H. Y. Low, Q. Ge, J. K. W. Yang, Structural multi-colour invisible inks with submicron 4D printing of shape memory polymers. *Nat. Commun.* **12**, 112 (2021).
- F. Wang, F. Luo, Y. Huang, X. Cao, C. Yuan, 4D printing via multispeed fused deposition modeling. *Adv. Mat. Technol.* **8**, 2201383 (2022).
- Q. Ge, C. K. Dunn, H. J. Qi, M. L. Dunn, Active origami by 4D printing. *Smart Mater. Struct.* **23**, 094007 (2014).
- Q. Ge, H. J. Qi, M. L. Dunn, Active materials by four-dimension printing. *Appl. Phys. Lett.* **103**, 131901 (2013).
- Z. Ding, C. Yuan, X. Peng, T. Wang, H. J. Qi, M. L. Dunn, Direct 4D printing via active composite materials. *Sci. Adv.* **3**, e1602890 (2017).
- A. Kotikian, R. L. Truby, J. W. Boley, T. J. White, J. A. Lewis, 3D printing of liquid crystal elastomeric actuators with spatially programmed nematic order. *Adv. Mater.* **30**, 1706164 (2018).
- B. Zhang, W. Zhang, Z. Zhang, Y. F. Zhang, H. Hingorani, Z. Liu, J. Liu, Q. Ge, Self-healing four-dimensional printing with an ultraviolet curable double-network shape memory polymer system. *ACS Appl. Mater. Interfaces* **11**, 10328–10336 (2019).
- Q. Ge, Z. Li, Z. Wang, K. Kowsari, W. Zhang, X. He, J. Zhou, N. X. Fang, Projection micro stereolithography based 3D printing and its applications. *Int. J. Extreme Manuf.* **2**, 022004 (2020).
- A. Kotikian, C. McMahan, E. C. Davidson, J. M. Muhammad, R. D. Weeks, C. Daraio, J. A. Lewis, Untethered soft robotic matter with passive control of shape morphing and propulsion. *Sci. Robot.* **4**, eaax7044 (2019).
- Y. Yang, Y. Chen, Y. Li, M. Z. Q. Chen, Y. Wei, Bioinspired robotic fingers based on pneumatic actuator and 3D printing of smart material. *Soft Robot.* **4**, 147–162 (2017).
- D. Montarnal, M. Capelot, F. Tournilhac, L. Leibler, Silica-like malleable materials from permanent organic networks. *Science* **334**, 965–968 (2011).
- B. Zhang, K. Kowsari, A. Serjouei, M. L. Dunn, Q. Ge, Reprocessable thermosets for sustainable three-dimensional printing. *Nat. Commun.* **9**, 1831 (2018).
- W. Zou, J. Dong, Y. Luo, Q. Zhao, T. Xie, Dynamic covalent polymer networks: From old chemistry to modern day innovations. *Adv. Mater.* **29**, 1606100 (2017).
- Q. Zhao, W. Zou, Y. Luo, T. Xie, Shape memory polymer network with thermally distinct elasticity and plasticity. *Sci. Adv.* **2**, e1501297 (2016).
- H. Song, Z. Fang, B. Jin, P. Pan, Q. Zhao, T. Xie, Synergetic chemical and physical programming for reversible shape memory effect in a dynamic covalent network with two crystalline phases. *ACS Macro Lett.* **8**, 682–686 (2019).
- Y. Shi, G. Fang, Z. Cao, F. Shi, Q. Zhao, Z. Fang, T. Xie, Digital light fabrication of reversible shape memory polymers. *Chem. Eng. J.* **426**, 131306 (2021).
- Y. Wang, Y. Pan, Z. Zheng, X. Ding, Reconfigurable and reprocessable thermoset shape memory polymer with synergetic triple dynamic covalent bonds. *Macromol. Rapid Commun.* **39**, e1800128 (2018).
- J. Joe, J. Shin, Y. S. Choi, J. H. Hwang, S. H. Kim, J. Han, B. Park, W. Lee, S. Park, Y. S. Kim, D.-G. Kim, A 4D printable shape memory vitrimer with repairability and recyclability through network architecture tailoring from commercial poly (*ε*-caprolactone). *Adv. Sci.* **8**, 2103682 (2021).
- Y. Zhang, N. Zheng, Y. Cao, F. Wang, P. Wang, Y. Ma, B. Lu, G. Hou, Z. Fang, Z. Liang, M. Yue, Y. Li, Y. Chen, J. Fu, J. Wu, T. Xie, X. Feng, Climbing-inspired twining electrodes using shape memory for peripheral nerve stimulation and recording. *Sci. Adv.* **5**, eaaw1066 (2019).
- B. Jin, H. Song, R. Jiang, J. Song, Q. Zhao, T. Xie, Programming a crystalline shape memory polymer network with thermo- and photo-reversible bonds toward a single-component soft robot. *Sci. Adv.* **4**, eaao3865 (2018).
- J. Ning, L. Huang, F. Zhao, W. Zhu, Y. Yang, F. Zeng, C. Tian, Q. Liu, J. Lv, M. Cui, X. Cai, W. Kong, Thermoset shape memory polymer with permanent shape reconfigurability based on dynamic disulfide bonds. *J. Polym. Res.* **29**, 278 (2022).
- N. Zheng, Z. Fang, W. Zou, Q. Zhao, T. Xie, Thermoset shape-memory polyurethane with intrinsic plasticity enabled by transcarbamoylation. *Angew. Chem.* **128**, 11593–11597 (2016).
- W. Miao, W. Zou, B. Jin, C. Ni, N. Zheng, Q. Zhao, T. Xie, On demand shape memory polymer via light regulated topological defects in a dynamic covalent network. *Nat. Commun.* **11**, 4257 (2020).
- B. Hao, Y. Li, X. Xiao, W. Dai, H. Chen, S. Chen, A facile photo-polymerization method for reconfigurable shape memory polymers. *Mater. Lett.* **254**, 214–217 (2019).
- Z. Fang, N. Zheng, Q. Zhao, T. Xie, Healable, reconfigurable, reprocessable thermoset shape memory polymer with highly tunable topological rearrangement kinetics. *ACS Appl. Mater. Interfaces* **9**, 22077–22082 (2017).
- W. Peng, G. Zhang, Q. Zhao, T. Xie, Autonomous off-equilibrium morphing pathways of a supramolecular shape-memory polymer. *Adv. Mater.* **33**, e2102473 (2021).
- M. I. Lawton, K. R. Tillman, H. S. Mohammed, W. Kuang, D. A. Shipp, P. T. Mather, Anhydride-based reconfigurable shape memory elastomers. *ACS Macro Lett.* **5**, 203–207 (2016).
- C. Cui, L. An, Z. Zhang, M. Ji, K. Chen, Y. Yang, Q. Su, F. Wang, Y. Cheng, Y. Zhang, Reconfigurable 4D printing of reprocessable and mechanically strong polythiourethane covalent adaptable networks. *Adv. Funct. Mater.* **32**, 2203720 (2022).
- J. T. Miao, M. Ge, S. Peng, J. Zhong, Y. Li, Z. Weng, L. Wu, L. Zheng, Dynamic imine bond-based shape memory polymers with permanent shape reconfigurability for 4D printing. *ACS Appl. Mater. Interfaces* **11**, 40642–40651 (2019).
- D. K. Patel, A. H. Sakhaei, M. Layani, B. Zhang, Q. Ge, S. Magdassi, Highly stretchable and UV curable elastomers for digital light processing based 3D printing. *Adv. Mater.* **29**, 1606000 (2017).
- Y. Shi, E. Askounis, R. Plamthottam, T. Libby, Z. Peng, K. Youssef, J. Pu, R. Peline, Q. Pei, A processable, high-performance dielectric elastomer and multilayering process. *Science* **377**, 228–232 (2022).
- R. Tomisawa, T. Ando, T. Ikaga, K. Kim, Y. Ohkoshi, K. Okada, H. Masunaga, T. Kanaya, H. Katsuta, Y. Funatsu, Ultra-SAXS observation of fibril-sized structure formation after the necking of poly (ethylene terephthalate) and poly (phenylene sulfide) fibers. *Polym. J.* **51**, 211–219 (2019).

46. Z. Fang, H. Song, Y. Zhang, B. Jin, J. Wu, Q. Zhao, T. Xie, Modular 4D printing via interfacial welding of digital light-controllable dynamic covalent polymer networks. *Matter* **2**, 1187–1197 (2020).
47. H. Li, B. Zhang, R. Wang, X. Yang, X. He, H. Ye, J. Cheng, C. Yuan, Y. F. Zhang, Q. Ge, Solvent-free upcycling vitrimers through digital light processing-based 3D printing and bond exchange reaction. *Adv. Funct. Mater.* **32**, 2111030 (2022).
48. S. Felton, M. Tolley, E. Demaine, D. Rus, R. Wood, A method for building self-folding machines. *Science* **345**, 644–646 (2014).
49. H. Ye, Q. Liu, J. Cheng, H. Li, B. Jian, R. Wang, Z. Sun, Y. Lu, Q. Ge, Multimaterial 3D printed self-locking thick-panel origami metamaterials. *Nat. Commun.* **14**, 1607 (2023).
50. J. Cheng, R. Wang, Z. Sun, Q. Liu, X. He, H. Li, H. Ye, X. Yang, X. Wei, Z. Li, B. Jian, W. Deng, Q. Ge, Centrifugal multimaterial 3D printing of multifunctional heterogeneous objects. *Nat. Commun.* **13**, 7931 (2022).

#### Acknowledgments

**Funding:** Q.G. acknowledges the National Natural Science Foundation of China (no. 12072142), the Key Talent Recruitment Program of Guangdong Province (no.

2019QN01Z438), and the support by the Science, Technology and Innovation Commission of Shenzhen Municipality under grant no. ZDSYS20210623092005017. H.L. acknowledges the National Natural Science Foundation of China (no. 52305312) and the Natural Science Foundation of Guangdong Province (no. 2022A1515010047). **Author contributions:** H.L. and Q.G. conceived the ideas and designed the research. H.L. and B.Z. developed materials. H.L. conducted majority of the experiments with assistance from H.Y., B.J., X.H., J.C., Z.S., R.W., and Z.C. H.L., B.Z., and Q.G. designed and analyzed SAXS experiments. J.L., R.X., and Q.L. contributed to the design of mechanical experiments. H.L. and Q.G. drafted and revised the manuscript. All authors discussed the results. **Competing interests:** The authors declare that they have no competing interests. **Data and materials availability:** All data needed to evaluate the conclusions in the paper are present in the paper and/or the Supplementary Materials.

Submitted 18 October 2023

Accepted 12 April 2024

Published 15 May 2024

10.1126/sciadv.adl4387